ADVANCED MATERIALS TECHNOLOGIES
www.advmattechnol.de

Cryptographic Strain-Dependent Light Pattern Generators

Francesca D'Elia, Francesco Pisani, Alessandro Tredicucci, Dario Pisignano, and Andrea Camposeo**

Refractive freeform components are becoming increasingly relevant for generating controlled patterns of light, because of their capability to spatially modulate optical signals with high efficiency and low background. However, the use of these devices is still limited by difficulties in manufacturing macroscopic elements with complex, 3D surface reliefs. Here, 3D-printed and stretchable magic windows generating light patterns by refraction are introduced. The shape and, consequently, the light texture achieved can be changed through controlled device strain. Cryptographic magic windows are demonstrated through exemplary light patterns, including micro-QR-codes, that are correctly projected and recognized upon strain gating while remaining cryptic for as-produced devices. The light pattern of micro-QR-codes can also be projected by two coupled magic windows, with one of them acting as the decryption key. Such novel, freeform elements with 3D shape and tailored functionalities is relevant for applications in illumination design, smart labels, anti-counterfeiting systems, and cryptographic communication.

1. Introduction

Controlling the spatial profile of light beams is critically important in various scientific and technological fields, including high-resolution microscopy,[1] endoscopy,[2] lithography and additive manufacturing,[3] optical manipulation of micro-objects,[4] wireless communication,[5] and computation.[6] Various methods have been reported to this aim, mostly based on diffractive elements and digital holography, which exploit arrays of micromirrors,[7] liquid crystal-based modulators,[8] or metasurfaces.[9]

While such techniques allow high spatial resolution in modulated beams as well as both static and dynamic light patterns to be generated, they typically need highly complex optical elements. This has recently pushed the attention toward refractive freeform optics that can redistribute the intensity profile from a light source into an arbitrary and predetermined pattern through simple and robust devices, in which at least one surface has no translational or rotational symmetry with respect to the axis normal to the component main plane.[10] The surfaces of freeform optical elements can be precisely designed to produce a desired intensity pattern,[11] defining the involved geometries as sum of spherical or aspherical lenses, or through Q-polynomials description and nonlinear partial differential equations.[10,12] The advantages of this method comprise relevant system miniaturization, wider field of view, and higher imaging resolution.[2,13,14] Manifold manufacturing technologies are generally required, involving grinding, polishing, and ultraprecision turning,[15,16] which is highly time-consuming, costly, and poorly versatile, thus preventing freeform optical systems to be realized rapidly and with features variable by external gates. Alternative manufacturing methods are available through 3D printing technologies that can generate objects with unprecedented complex geometries.[17–19] 3D printing comprises a variety of processes to fabricate unconventional architectures by different materials.[20–22] In the field of optics and optoelectronics, additive manufacturing has been already employed to produce aspheric lenses, micro-optics, waveguides, photonic crystals, light-emitting diodes (LEDs), detectors, and sensors.[19,23,24] Though 3D printing of macroscopic objects with optical quality and sub-micrometric resolution is still challenging,[25] a number of approaches have been proposed for improving the achievable accuracy, as well as the rate of printing and the size of the printed objects.[26–28] Importantly, some applications might exploit light patterns generated from surfaces with lower quality, taking advantage of the design flexibility and customization offered by 3D printing technologies. A relevant example is given by cryptographic labels,[29,30] where the capability to recognize the generated light patterns by naked eye or by a low-cost scanner, without the need of bulky optics and complex optical systems, is highly desirable.[31,32]

F. D'Elia
NEST
Scuola Normale Superiore
Piazza S. Silvestro 12, Pisa I-56127, Italy
F. Pisani, A. Tredicucci, D. Pisignano
Dipartimento di Fisica
Università di Pisa
Largo B. Pontecorvo 3, Pisa I-56127, Italy
E-mail: francesco.pisani@df.unipi.it
A. Tredicucci, D. Pisignano, A. Camposeo
NEST
Istituto Nanoscienze-CNR and Scuola Normale Superiore
Piazza S. Silvestro 12, Pisa I-56127, Italy
E-mail: andrea.camposeo@nano.cnr.it

The ORCID identification number(s) for the author(s) of this article can be found under https://doi.org/10.1002/admt.202101129.

DOI: 10.1002/admt.202101129

Furthermore, additive manufacturing combined with flexible materials, such as polymeric elastomers, might lead to optical components with high compliance to nonplanar surfaces and large strain.[33] In this respect, compression, bending, or stretching, exploited so far for tuning deformable photonic devices,[34–36] could be rethought as effective gating fields to provide 3D optical systems with new functionalities, including controllable properties and cryptographic capability.

Here, we introduce 3D-printed stretchable magic windows (MWs).[37] MWs are transparent refractive components whose surface reliefs are designed by the inverse Laplacian of a target light pattern[37] and are capable to reshape an incoming light beam into the target image. Our MWs are manufactured by digital light processing (DLP), a fast and cheap 3D printing technology (see the Experimental Section for details). The 3D-printed MWs, assessed through the achieved spatial distribution of the light intensity, evidence the possibility to design the desired shape of a transmitted optical beam in the whole visible range. Cryptographic systems are demonstrated, in which the information (micro-QR-codes) carried by a light pattern is encrypted in 3D shaped MWs and unveiled by projection of the light pattern through coupled MWs. Moreover, stretchable MWs are made by replica molding of the 3D-printed optics, finding that the resulting light pattern can be varied across pre-configured geometries by the application of uniaxial strain to MW elastomers. More specifically, MWs can be designed to project indecipherable patterns, whose encoded information (micro-QR-codes) controllably becomes readable upon applying a calibrated uniaxial strain to the devices.

2. Results and Discussion

The working principle of MWs is illustrated in **Figure 1**a: it relies on the refraction of light passing through a textured interface between two media with different refractive index. As schematized in the inset of Figure 1a, the incident light rays are deflected by a certain angle, which depends on the surface texture and the refractive index mismatch. The refracted rays, collected at a defined "focal" distance, f_{MW}, produce a specific spatial distribution of the light intensity. Given the intensity pattern to be realized, the surface profile of the MW can be calculated by solving the inverse problem, for which various approaches have been reported.[16]

Here the method proposed in ref. [37] is followed: given the desired distance between the plane of projection of the image and the MW (f_{MW}), the MW surface profile $h(x,y)$ (where x,y are the in-plane coordinates and h is the thickness of the MW, Figure 1b) can be calculated by solving the inverse Laplacian of the target light pattern, I (more details about the design and realization of the MWs are reported in the Experimental Section and in Figure S1, Supporting Information)[37]

$$\nabla^2 h(R) = \frac{1}{\left(I(R)-1\right) f_{MW}\,(n-1)} \tag{1}$$

where $R = \{x,y\}$, and n is the refractive index ($n = 1.5$ in our calculations). From Equation (1), the surface profile $h(x,y)$ is calculated by finite difference approach (see the Experimental Section for details) and used for the design of the 3D MW by computer assisted design (CAD).

Figure 1b shows an example of the calculated surface profile of the MW for the target pattern shown in the inset. The corresponding 3D-printed MW is shown in Figure 1c. The MW is almost transparent in the visible range (optical attenuation data are shown in Figure S2, Supporting Information) and has no pattern on its surface which is discernible to the naked eye. Importantly, at variance with diffractive architectures and metasurfaces, the overall technology is entirely based on geometrical optics, thus leading to

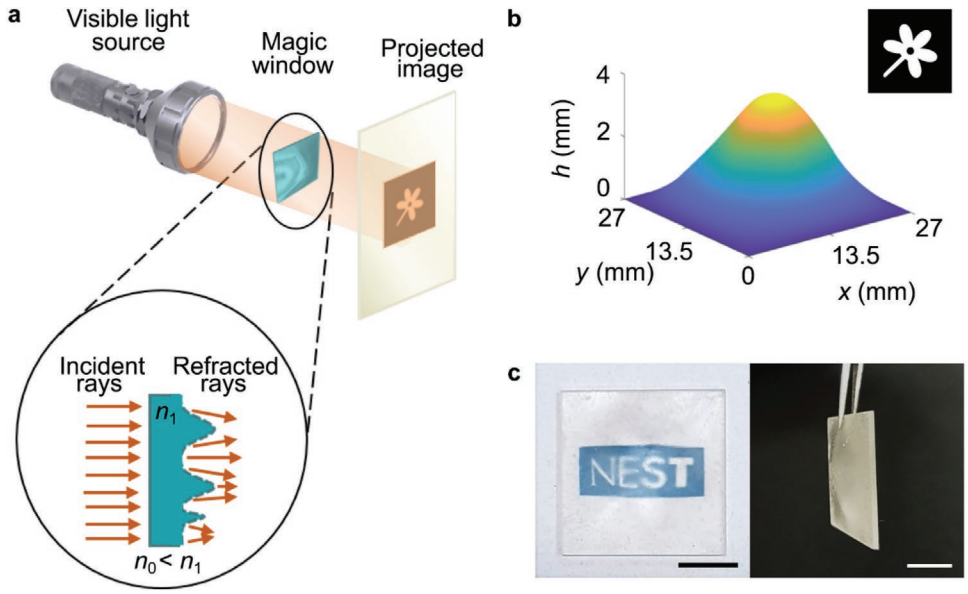

Figure 1. 3D-printed MWs. a) Scheme of the MW working principle: light rays from a visible light source are refracted by the MW, whose surface profile is designed to generate the target pattern on a screen placed at the focal distance. Inset: scheme of refracted light rays travelling through a textured interface between two media with different refractive indexes (n_1 and n_0 for the MW and the surrounding medium, respectively). b) Calculated 3D surface profile of a MW which projects a pattern with a flower (inset). c) Photographs of a 3D-printed MW, showing high transparency on top of the NEST Logo (left), and viewed from its side on black background (right). Scale bars: 1 cm.

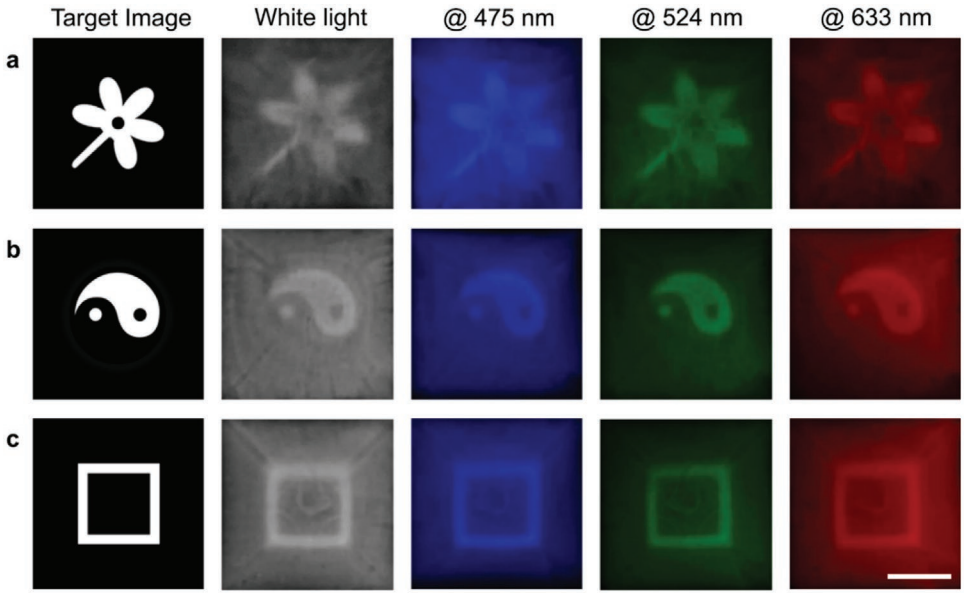

Figure 2. Cast images with different visible light sources. a–c) Target images (left side), and photographs of the images cast by the MWs when illuminated with different LEDs. The images are projected on a screen placed at ≈3 mm and captured with a photocamera placed behind the screen. Scale bar: 1 cm.

wavelength-independent components made of transparent materials which might exhibit unequalled broadband operation.

Several MWs are designed and printed, with different target patterns: a flower, a Yin Yang symbol, and a square perimeter (**Figure 2**). They are illuminated with various LED sources (Figure S3, Supporting Information, and the Experimental Section for details), and the corresponding light patterns projected on a screen are shown in Figure 2, evidencing that the 3D-printed MWs can reproduce the desired intensity patterns with high accuracy at several different wavelengths. All images in Figure 2 are obtained at the same focal distance, although this aspect can be in principle affected by the wavelength dispersion of the refractive index of the photo-polymerized MW material (1.48–1.58 for visible light).[38]

The variation of the light patterns as a function of the distance, d, from the MW is shown in **Figure 3**a–d. Taking the target image as reference (Figure 3a,c), the patterns projected on the screen are better reproduced, in terms of shape and contrast, when the screen is positioned at $d = 3$ mm from the MW. The intensity micrographs collected by a CMOS camera (active area 6.66×5.32 mm^2, Figure 3c,d) is in agreement with the results of the performed ray tracing simulations for various d values (Figure S4, Supporting Information).

The properties of the light pattern cast by the MWs are evaluated by three figures of merits: the full width at half maximum (FWHM) of a selected feature (the flower stem in Figure 3), and two contrast parameters, i.e., the contrast-to-noise ratio (CNR) and the Weber contrast (WC), defined as follows

$$CNR = \frac{\langle I_W \rangle - \langle I_B \rangle}{(\sigma_W + \sigma_B)/2} \quad (2)$$

$$WC = \frac{\langle I_W \rangle - \langle I_B \rangle}{\langle I_B \rangle} \quad (3)$$

where $\langle I_W \rangle$, $\langle I_B \rangle$, σ_W, and σ_B are the average intensity and standard deviation of light intensity of the white and black regions, respectively (red squares in Figure 3c). WC is a measure of the image contrast normalized to the background luminosity, whereas CNR takes into account also the noise of the image.[39,40] In Figure 3e, the intensity profile of a detail of the projection (red line in Figure 3c) is shown as a function of the distance, d. From such data the FWHM of the investigated feature as a function of d is obtained (Figure 3f). The measured size of the flower stem image is found to match the size of the corresponding feature of the target image at $d = 3$ mm, in accordance with the value of f_{MW} used for the MW design. Figure 3g shows the d-dependence of the contrast parameters, both featuring a maximum at $d = 3$ mm, in agreement with the analysis of the feature width. Similar results are obtained for the other studied patterns (Figure S5, Supporting Information).

To investigate the minimum feature size that can be projected by the MWs printed by DLP, a set of samples designed for projecting patterns with various geometries (squares and parallel lines) and with features size ranging from 5 mm down to 100 µm are realized (Figure S6, Supporting Information). The corresponding projected light patterns upon white light illumination are shown in Figure S6 (Supporting Information). The analysis of the WC and CNR parameters (Figure S7, Supporting Information) performed on arrays of horizontal and vertical parallel lines (Figure S6d, Supporting Information) highlights that patterns with feature size down to 300 µm are projected clearly and without appreciable artefacts. The main limitation of the MWs here realized relies on their stepped surface profile (Figures S8 and S9, Supporting Information), which impacts more relevantly on features with smaller size which typically have also smaller height (Figure S10, Supporting Information). The stepped surface profile of the MWs has the main effect of decreasing the contrast of projected features as shown in Figure S11 (Supporting Information), where the

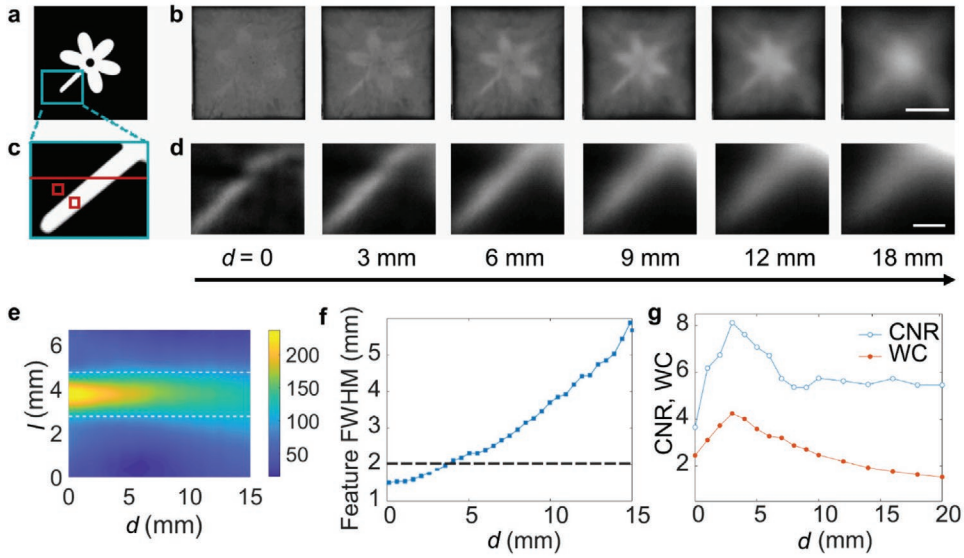

Figure 3. Quantitative analysis of MW projection. a) Target image. b) Photographs of the projected images at different distances, *d*, of the screen with respect to the MW. $d = 0$ corresponds to the MW touching the projection screen. Scale bar: 1 cm. Here, blurring and contrast are mostly determined by diffusion and absorption by the semi-transparent screen. c) Feature chosen for the measurements with the CMOS camera. d) Maps of the intensity acquired by positioning the CMOS camera at different distances, *d*, from the MW. Scale bar: 2 mm. e) 2D map of the light intensity profile versus the distance, *d*, and the coordinate, *l*, along the red line in (c). The dashed lines mark the theoretical size of the flower stem. f) Size of the flower stem (FWHM of the intensity profile) versus *d*. The dashed horizontal line corresponds to the width of the feature of the target image. g) CNR (empty circle) and WC (full circle) versus *d*. CNR and WC are calculated using the areas highlighted with red boxes in (c).

patterns projected by a smooth and by a stepped surface profile of the MWs are compared. Other parameters of the MWs that affect their height profile are the f_{MW} value, and their lateral size, the thickness of the MW being proportional to the latter and inversely proportional to f_{MW}. Such trends allow us to calculate the dependence of the thickness of individual layers for a MW that is sliced in 100 layers as a function of f_{MW} and of the lateral size (Figure S12, Supporting Information), and to compare the obtained values with the spatial resolution of various 3D printing technologies. Indeed, current 3D printing methods provide for a wide range of spatial resolutions,[28] and the most suitable technique can be selected depending on the designed MW features. As a general trend, MWs with longer focal distance and smaller lateral size require 3D printing with higher spatial resolution, such as multiphoton stereolithography.[41] Less stringent requirements for spatial resolution are needed for MWs having larger lateral size and shorter focal distances (Figure S12, Supporting Information).

To add a new dimension to freeform optical elements, mechanically deformable MWs are realized made of polydimethylsiloxane (PDMS), by replica molding from the 3D-printed MW templates (**Figure 4**a). The PDMS MW has 3D surface reliefs corresponding to the negative of the template, and thus projects an image with black and white areas inverted with respect to the starting 3D-printed MW. Therefore, the mold templates are designed and printed to cast

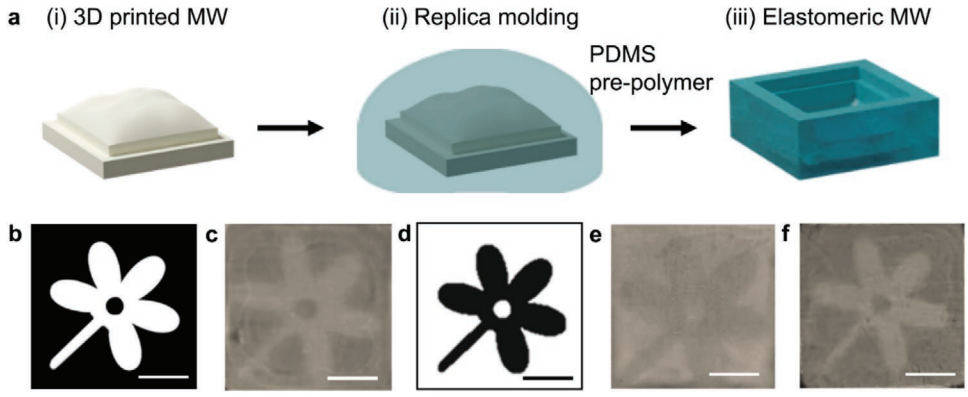

Figure 4. Elastomeric MWs. a) Schematic view of the replica molding process of the elastomeric MWs. A template is 3D-printed (i) and covered with PDMS pre-polymer (ii), which is then cured. The resulting elastomeric MW (iii) is peeled off from the substrate. b) Target image and c) corresponding image projected by the 3D-printed MWs. d) Target image with inverted black and white areas with respect to the one shown in (b). Corresponding images projected by the e) 3D-printed MW and f) PDMS replica, realized starting from (e). Scale bars: 1 cm.

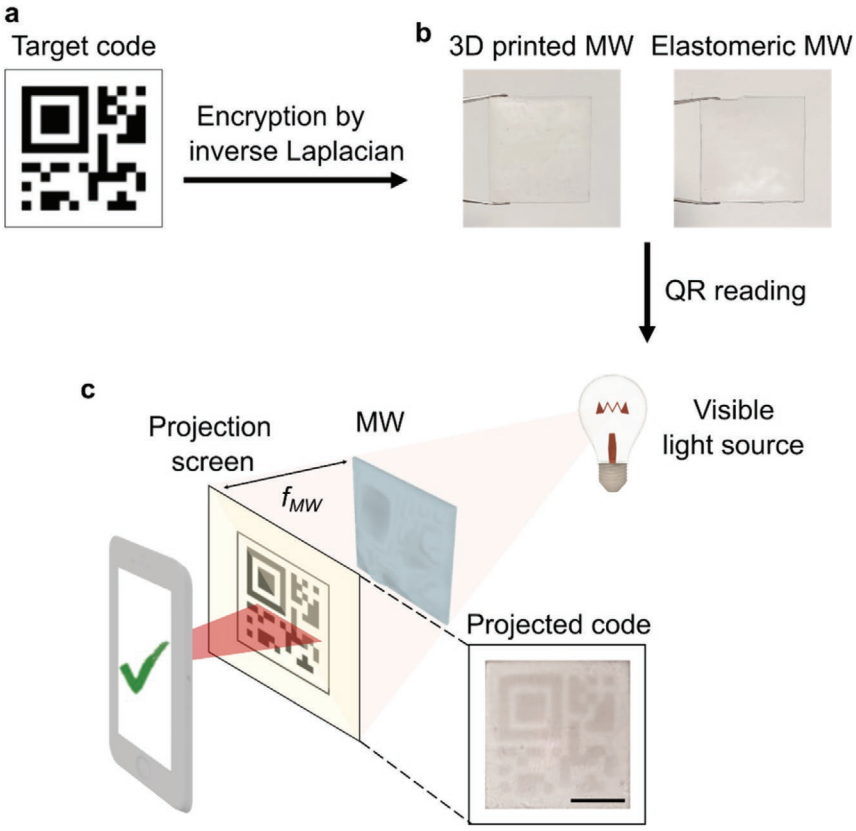

Figure 5. a) Target image of a micro-QR-code encoded with the letters "ABVZ." b) Photographs of the MWs realized by 3D printing (left image) and replica molding (right image) methods. MW lateral size = 27 × 27 mm^2. c) Scheme of the QR reading mechanism based on the illumination of the MW by a broadband light source and the projection of the crypted pattern on a screen. The projected pattern can be read by a QR scanner. The inset shows an example of the pattern projected by a MW realized starting from the image shown in (a). Scale bar: 1 cm.

patterns with inverted black and white areas with respect to the desired image (Figure 4d,f and Experimental Section for details). The obtained elastomeric MWs project images with lower background compared to the 3D-printed ones (Figure 4f vs Figure 4c), because of the reduced bulk light scattering from PDMS that determines lower attenuation in the visible range (Figure S2, Supporting Information). Hence, elastomeric MWs generally outperform 3D-printed templates in terms of the obtained image quality and contrast (Figures S6 and S7, Supporting Information). A variation of the patterns generated from the PDMS MW similar to the 3D-printed one is found upon increasing the distance, d (Figure S13, Supporting Information).

MWs have the interesting property to unveil a structured pattern on a screen positioned at a well-defined distance (f_{MW}) when illuminated. We exploit this property by realizing cryptographic MWs designed to project the complex pattern of a micro-QR-code encoded with the letters "ABVZ" (**Figure 5**a). The micro-QR-codes can be encrypted in the topography of MWs through the calculation of the inverse Laplacian, while the feature of the topography of both printed and elastomeric MWs (almost invisible to naked eyes) cannot reveal the code content (Figure 5b). The reading of the QR-codes is then carried out by illuminating the MWs and projecting the crypted pattern on a screen at f_{MW} distance (Figure 5c).

The above encryption mechanism can be further strengthened by utilizing two coupled MWs, whose encrypted light pattern can be unveiled only if the two optical components are placed in series, while remaining undecipherable if only one of them is used (**Figure 6**). In such approach, one of the two MWs acts as unique key for decryption.

Finally, the surface morphology of elastomeric MWs can be varied by mechanical elongation, thus opening the possibility to modify the resulting light pattern generated by controlling the device stretching. This property can be exploited as an additional degree of encryption of the information carried by the MW. To this aim, elastomeric MWs are designed starting from a pattern of the micro-QR code that is intentionally encrypted in a way that it cannot be read by a QR scanner unless a predefined uniaxial strain, $\varepsilon = \Delta L/L_0$ (where L_0 is the lateral size of the unstretched MW) is applied (**Figure 7**a,b). We realize two MWs textured with different surface profiles, namely, designed to work upon calibrated elongation of 15–20% (Figure 5c) and of 20–30% (Figure 7d), respectively. Slight reductions of the set elongation points might be related to the algorithms exploited for error correction by QR scanners, and to possible damage or deformation compensation of the 2D code pattern.[42,43] An exemplary behavior of the MW under stretching is also shown in Movie S1 (Supporting Information).

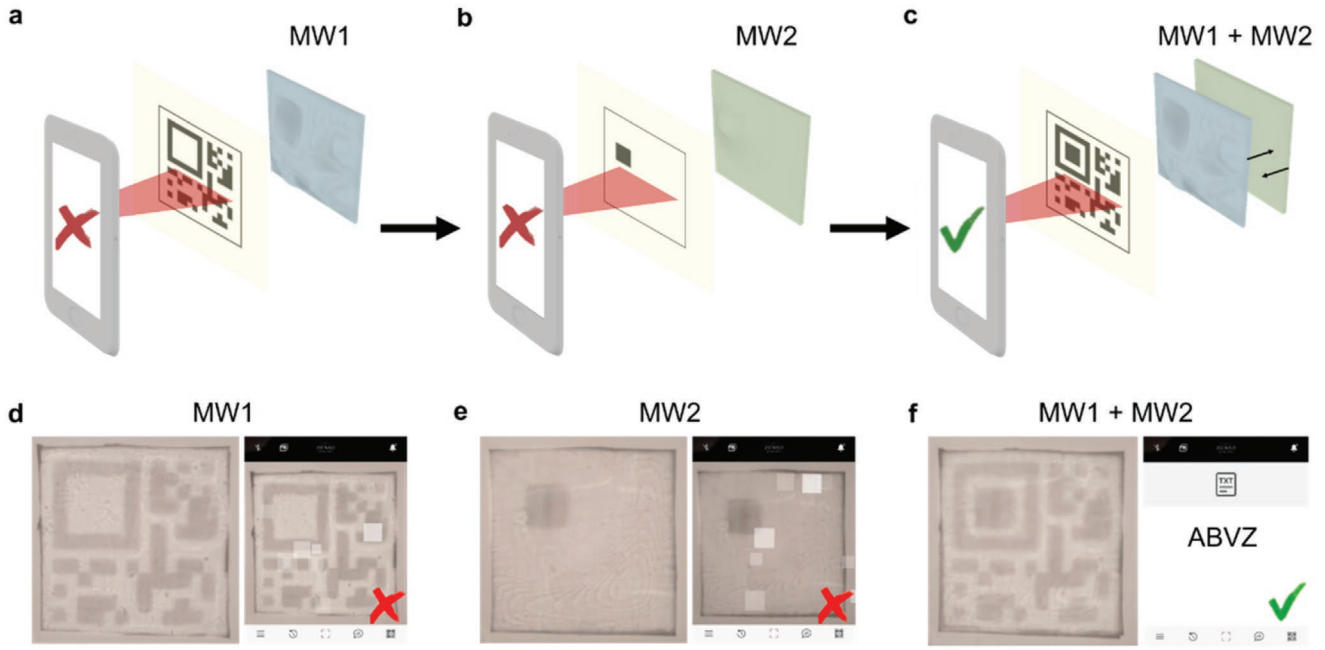

Figure 6. Cryptographic MW with decryption key. a-c) Schematic illustration of the operation of two coupled cryptographic MWs (MW1 and MW2). The projected pattern is unreadable when a single MW is used (a, b), while becoming readable when they are in series (c). Photographs (left side of each panel) of the patterns projected by the cryptographic elastomeric d) MW1, e) MW2, and f) by the combination of the two. On the right side of (d–f) the screenshot of the QR scanner is shown. The pattern of gray squares in (e) and (f) is due to the graphic interface of the QR scanner.

The above results highlight the potential of 3D printing for the versatile manufacturing of cryptographic elements. MWs with surface reliefs are capable of redirecting light rays from sources with different wavelengths, to form predetermined patterns at a well-defined focal distance. Elastomeric MWs constitute a novel platform combining freeform surface design, shape and architecture tailorable by controlled mechanical deformation, and optical multifunctionality, encoded through the different 3D shapes that the optical component can acquire in response to an external stimulus (here, uniaxial strain). Such combination results in the possibility to vary the cast patterns, switching from unreadable to readable pictures in a reversible way upon encoding information in the 3D shape of the freeform optical component.

3. Conclusion

In summary, we introduced cryptographic, 3D optical components capable of projecting a predefined light pattern, upon illumination with light in the visible range, including white sources. Enhanced by inverse Laplacian design and replication methods as done in this work, DLP can also enable the fabrication of freeform elements with stretchable materials.[3,44] We anticipate that 3D-printed MWs might be also used for large-scale, broadband beam shaping and control, which is especially useful in those spectral intervals where beam shaping is more demanding, such as for the THz or mid-IR wavelengths. For such spectral ranges, the larger wavelengths would also lead to less stringent requirements of printing to achieve high-quality optical surfaces, and various stereolithographic methods are currently available to this aim.[28] Printable resins with low attenuation losses in these spectral ranges have been recently demonstrated[45] and could be used for the additive manufacturing of high-quality, freeform optical systems. Stretchable MWs with tailored functionality might find application in fields such as illumination design, smart labels, anti-counterfeiting, and cryptographic systems.

4. Experimental Section

Calculation of the Surface Relief of the MW: Given a generic freeform interface with sufficiently gentle height variation, the intensity profile, $I(R)$, that is generated by the refraction of incident light rays satisfies the following relation[37]

$$I(R) = \frac{1}{1 + f_{MW}(n-1)\nabla^2 h(R)} \tag{4}$$

Equation (4) provides us with a direct relation between the intensity profile of the image to be projected and the height of the surface of the MW, $h(R)$, as reported in Equation (1).

To find $h(R)$ one has to solve the inverse Laplacian of Equation (1), which can be done numerically with a finite difference approach

$$h(i,j) = \frac{1}{4}\left[-\nabla^2 h(i,j)\delta x \delta y + h(i-1,j) + h(i,j-1) + h(i+1,j) + h(i,j+1)\right] \tag{5}$$

where $\delta x = x(i+1) - x(i)$ and $\delta y = y(j+1) - y(j)$, respectively. We point out that the target image is a digital image composed by a finite number of pixels, and i, j are the indexes of the pixel in the ith row and jth column, respectively. The values of the height profile are found starting from the calculation of the right side of Equation (4) at a point $R(i,j) = \{x(i), y(j)\}$. Equation (5) must be solved for every $x(i)$, $y(j)$ and the process must be iterated until it reaches convergence. The boundary conditions are

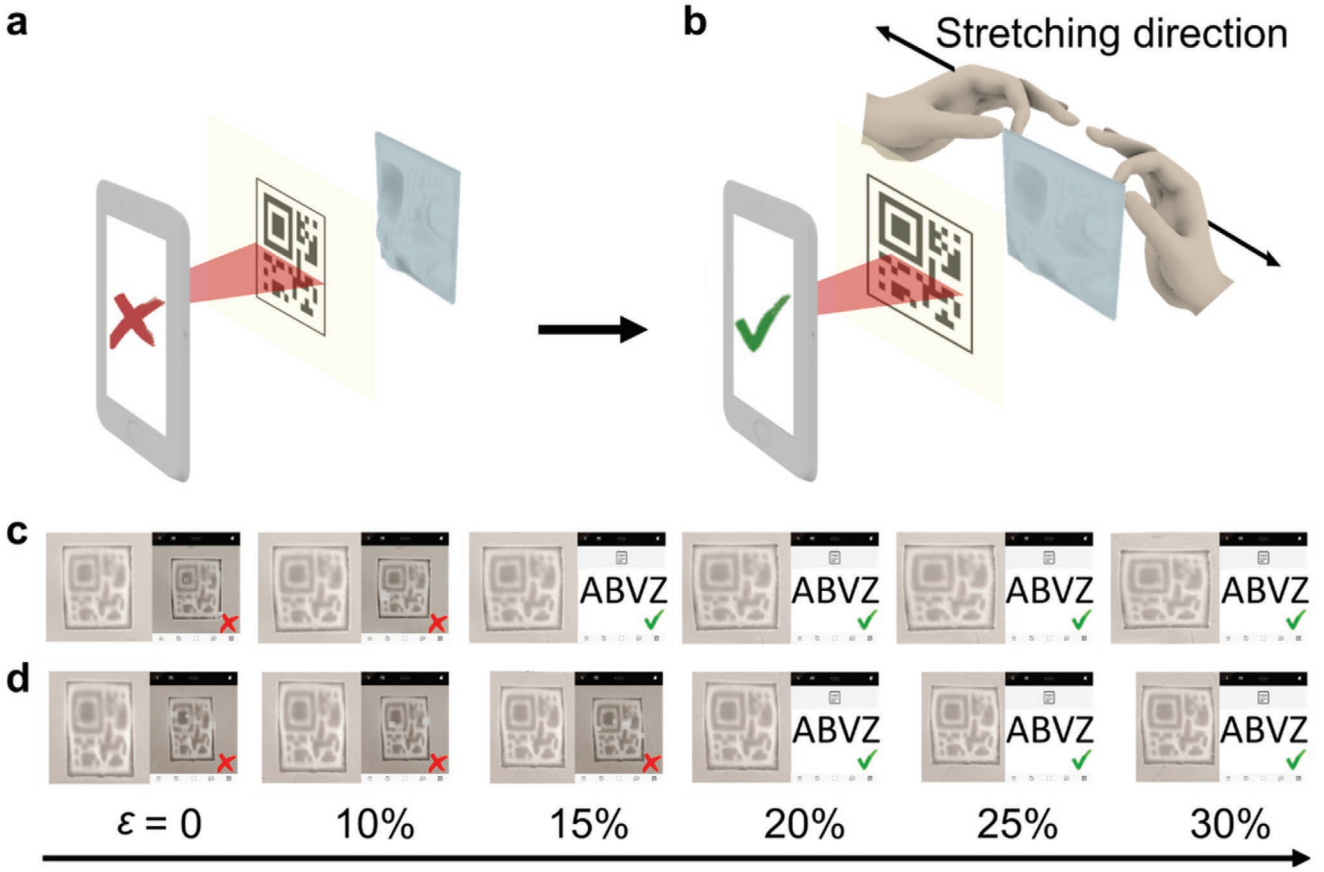

Figure 7. Deformable elastomeric MWs. a,b) Illustration of the working principle of stretchable cryptographic MWs. The obtained light pattern is controlled by the mechanical deformation and made readable by a smartphone scanner only upon applying a calibrated stretching. c,d) Photographs (left side of the pictures) of the patterns projected by the controllably elongated elastomeric MWs undergoing uniaxial strains, ε, increasing from 0 to 30% from left to right. On the right side of each picture the screenshot of the QR scanner is shown, highlighting images which are decoded by the scanner.

chosen to zero the height of the surface at the edges. Moreover, the intensity of the image must be normalized with the window area

$$\int_{\{x,y\}=0}^{\{x,y\}=L} I(x,y)dxdy = A = L^2 \tag{6}$$

with L the side length of the MW (here assumed to be squared). If this step is not performed the height profile is superimposed on a concave or convex parabolic profile.[37] Indeed, the possibility of modifying the surface relief of the MW, by considering a normalization constant in Equation (6) $A > L^2$ ($A < L^2$) for a convex (concave) shape gives an additional flexibility for the design of the MW, which can be better tailored to the 3D printing process. In fact, this normalization method is exploited to further engineer the MW and create a convex profile, which is important because the convex shape prevents the air from getting stuck under the previously printed layers, creating bubbles and ripples in the final 3D-printed MW (Figure S14, Supporting Information). The variation of the normalization constant, A, has two consequences: i) the focal distance will slightly decrease (increase) due to the superimposed convex (concave) profile which changes the angle of incidence on the surface features; and ii) the contrast between black and white areas of the projected intensity profile will slightly decrease as the black regions in the digital image will now become gray.

To design the stretchable MW, one has to consider that the replica molding results in a PDMS MW with an inverted surface profile with respect to the 3D-printed template. Therefore, the PDMS MW will project the same image but with black and white areas inverted. To realize a PDMS MW that projects the original image, the template MW was designed and 3D-printed starting from a negative target image. The flexible MW can be also designed to project a distorted image, for example, shrunken in one direction, so that the undistorted, desired image can be obtained by uniaxial stretching of the MW. To this aim, the thinning of the material when stretched has to be accounted for. The relation between the stretched length and the height variation can be derived through the Poisson's ratio, ν, of the deformable material

$$\nu = -\frac{(h-h_0)/h_0}{(L-L_0)/L_0} \tag{7}$$

where h_0 and L_0 are the thickness and length at rest, h and L are the corresponding stretched values, respectively ($\nu = 0.49$ for PDMS).[46] The surface profile of the MW is firstly calculated for the undistorted image, and then shrunk along one axis, e.g., the x axis, by a certain percentage. The thickness of the deformed MW is then derived through Equation (7).

3D-Printed and Elastomeric MWs: The MWs were printed by using the E-shell 600 (ENVISIONTEC) photo-polymer. The MWs were printed by using the Micro Plus HD (ENVISIONTEC) system, a DLP 3D printer with a maximum printing volume of 45 × 28 × 100 mm^3, by setting a thickness of single layers of 15 µm (Figures S8 and S9, Supporting Information). After printing, the MWs were rinsed in isopropanol, dried under a nitrogen flow, and inspected by optical microscopy by using an upright stereomicroscope (MZ16 FA, Leica) and a bright field microscope (BX52, Olympus). In addition, the features of the 3D-printed MWs were imaged by scanning electron microscopy (SEM, Merlin, Zeiss) and by an optical profilometer (Talysurf CCI, Taylor Hobson Precision). To this aim, a thin layer of Cr (thickness 20 nm) was thermally evaporated on the

MW surface. Optical transmittance spectra were measured by using a Lambda 950 spectrophotometer (Perkin Elmer). Elastomeric MWs were fabricated using a PDMS pre-polymer (Sylgard 184, Dow Corning) by mixing the base and the curing agent with a 9:1 weight:weight ratio. The resulting mixture was degassed in vacuum for 1 h to remove air bubbles, and poured in a Petri dish containing the 3D-printed MWs. Once the crosslinking of the PDMS was completed (typically after 48 h at room temperature), the replica is peeled off.

Characterization: The properties of 3D-printed and stretchable MWs were assessed by projection experiments. The printed MWs were mounted on a micrometric translation stage and illuminated with either an incandescent light bulb with variable intensity or a white emitting LED, and with different LEDs with emission wavelength peaked at 475, 524, and 633 nm, respectively. The pattern generated by the MWs was projected on a polyethylene screen (optical transmission spectrum in Figure S15, Supporting Information) and captured with a photocamera placed on the opposite side of the screen (Figure S3, Supporting Information). To record the intensity distribution of the cast light pattern, the screen was replaced by a CMOS camera (Thorlabs). For testing the MWs under stretching, they were locked between two clamps mounted on microtranslators which allow samples to be stretched along one direction.

Supporting Information

Supporting Information is available from the Wiley Online Library or from the author.

Acknowledgements

F.D'E. and F.P. contributed equally to this work. The research leading to these results received funding from the European Research Council (ERC) under the European Union's Horizon 2020 research and innovation programme (Grant Agreement No. 682157, "*x*PRINT") and from the Italian Minister of University and Research PRIN 2017PHRM8X project. A.P. and L.R. are gratefully acknowledged for profilometer characterization and SEM images, respectively.

Open access funding provided by Consiglio Nazionale delle Ricerche within the CRUI-CARE Agreement.

Conflict of Interest

The authors declare no conflict of interest.

Data Availability Statement

The data that support the findings of this study are available from the corresponding author upon reasonable request.

Keywords

3D printing, additive manufacturing, cryptographic systems, freeform components, stretchable devices

Received: August 30, 2021
Published online: October 19, 2021

[1] J. Tang, J. Ren, K. Y. Han, *Nanophotonics* **2019**, *8*, 2111.
[2] F. Duerr, Y. Meuret, H. Thienpont, *Opt. Express* **2013**, *21*, 31072.
[3] P. Kunwar, A. V. S. Jannini, Z. Xiong, M. J. Ransbottom, J. S. Perkins, J. H. Henderson, J. M. Hasenwinkel, P. Soman, *ACS Appl. Mater. Interfaces* **2020**, *12*, 1640.
[4] F. Nan, Z. Yan, *Nano Lett.* **2019**, *19*, 3353.
[5] Z. Cao, X. Zhang, G. Osnabrugge, J. Li, I. M. Vellekoop, A. M. Koonen, *Light Sci. Appl.* **2019**, *8*, 69.
[6] M. W. Matthès, P. del Hougne, J. de Rosny, G. Lerosey, S. M. Popoff, *Optica* **2019**, *6*, 465.
[7] P. Zupancic, P. M. Preiss, R. Ma, A. Lukin, M. E. Tai, M. Rispoli, R. Islam, M. Greiner, *Opt. Express* **2016**, *24*, 13881.
[8] A. Forbes, A. Dudley, M. McLaren, *Adv. Opt. Photonics* **2016**, *8*, 200.
[9] J. Scheuer, *Nanophotonics* **2017**, *6*, 137.
[10] H. Ries, J. Muschaweck, *J. Opt. Soc. Am. A* **2002**, *19*, 590.
[11] R. Wu, Z. Feng, Z. Zheng, R. Liang, P. Benítez, J. C. Miñano, F. Duerr, *Laser Photonics Rev.* **2018**, *12*, 1700310.
[12] I. Kaya, J. P. Rolland, *Adv. Opt. Technol.* **2013**, *2*, 81.
[13] R. Völkel, M. Eisner, K. J. Weible, *Microelectron. Eng.* **2003**, *67*, 461.
[14] E. Muslimov, E. Hugot, W. Jahn, S. Vives, M. Ferrari, B. Chambion, D. Henry, C. Gaschet, *Opt. Express* **2017**, *25*, 14598.
[15] T. Blalock, K. Medicus, J. D. Nelson, *Proc. SPIE* **2015**, *9575*, 95750H.
[16] R. Wu, L. Xu, P. Liu, Y. Zhang, Z. Zheng, H. Li, X. & Liu, *Opt. Lett.* **2013**, *38*, 229.
[17] D. L. Bourell, *Annu. Rev. Mater. Res.* **2016**, *46*, 1.
[18] J. del Barrio, C. Sánchez-Somolinos, *Adv. Opt. Mater.* **2019**, *7*, 1900598.
[19] A. Camposeo, L. Persano, M. Farsari, D. Pisignano, *Adv. Opt. Mater.* **2019**, *7*, 1800419.
[20] S. C. Ligon, R. Liska, J. Stampfl, M. Gurr, R. Mülhaupt, *Chem. Rev.* **2017**, *117*, 10212.
[21] Z. C. Eckel, C. Zhou, J. H. Martin, A. J. Jacobsen, W. B. Carter, T. A. Schaedler, *Science* **2016**, *351*, 58.
[22] R. L. Truby, J. A. Lewis, *Nature* **2016**, *540*, 371.
[23] H. Y. Jeong, E. Lee, S. An, Y. Lim, Y. C. Jun, *Nanophotonics* **2020**, *9*, 1139.
[24] S. Schmidt, S. Thiele, A. Toulouse, C. Bösel, T. Tiess, A. Herkommer, H. Gross, H. Giessen, *Optica* **2020**, *7*, 1279.
[25] N. Vaidya, O. Solgaard, *Microsyst. Nanoeng.* **2018**, *4*, 18.
[26] J. R. Tumbleston, D. Shirvanyants, N. Ermoshkin, R. Januszewicz, A. R. Johnson, D. Kelly, K. Chen, R. Pinschmidt, J. P. Rolland, A. Ermoshkin, E. T. Samulski, J. M. DeSimone, *Science* **2015**, *347*, 1349.
[27] X. Chen, W. Liu, B. Dong, J. Lee, H. O. T. Ware, H. F. Zhang, C. Sun, *Adv. Mater.* **2018**, *30*, 1705683.
[28] V. Hahn, P. Kiefer, T. Frenzel, J. Qu, E. Blasco, C. Barner-Kowollik, M. Wegener, *Adv. Funct. Mater.* **2020**, *30*, 1907795.
[29] R. Chen, D. Feng, G. Chen, X. Chen, W. Hong, *Adv. Funct. Mater.* **2021**, *31*, 2009916.
[30] W. Ren, G. Lin, C. Clarke, J. Zhou, D. Jin, *Adv. Mater.* **2020**, *32*, 1901430
[31] X. Zheng, Y. Zhu, Y. Liu, L. Zhou, Z. Xu, C. Feng, C. Zheng, Y. Zheng, J. Bai, K. Yang, D. Zhu, J. Yao, H. Hu, Y. Zheng, T. Guo, F. Li, *ACS Appl. Mater. Interfaces* **2021**, *13*, 15701.
[32] H.-Y. Wang, K.-K. Yu, C.-Y. Tan, K. Li, Y.-H. Liu, L. Shi, K. Lu, X.-Q. Yu, *J. Mater. Chem. C* **2021**, *9*, 2864
[33] S. Geiger, J. Michon, S. Liu, J. Qin, J. Ni, J. Hu, T. Gu, N. Lu, *ACS Photonics* **2020**, *7*, 2618.
[34] S. C. Malek, H. S. Ee, R. Agarwal, *Nano Lett.* **2017**, *17*, 3641.
[35] J. Wang, Y. Yin, Q. Hao, S. Huang, E. S. G. Naz, O. G. Schmidt, L. Ma, *ACS Photonics* **2018**, *5*, 2060.
[36] S. Petsch, S. Schuhladen, L. Dreesen, H. Zappe, *Light: Sci. Appl.* **2016**, *5*, e16068.

[37] M. V. Berry, *J. Opt.* **2017**, *19*, 06LT01.
[38] F. Aloui, L. Lecamp, P. Lebaudy, F. Burel, *Express Polym. Lett.* **2018**, *12*, 966.
[39] W. B. Thompson, G. E. Legge, D. J. Kersten, R. A. Shakespeare, Q. Lei, *J. Opt. Soc. Am. A* **2017**, *34*, 583.
[40] R. N. Bryan, *Introduction to the Science of Medical Imaging*, Cambridge University Press, Cambridge **2009**.
[41] J. Fischer, M. Wegener, *Laser Photonics Rev.* **2013**, *7*, 22.
[42] L. Jeng-An, F. Chiou-Shann, *Math. Probl. Eng.* **2013**, *2013*, 848276.
[43] L. Karrach, E. Pivarčiová, P. Božek, *J. Imaging* **2020**, *6*, 67.
[44] Z. Hong, R. Liang, *Sci. Rep.* **2017**, *7*, 7145.
[45] F. Zhou, W. Cao, B. Dong, T. Reissman, W. Zhang, C. Sun, *Adv. Opt. Mater.* **2016**, *4*, 1034.
[46] A. Müller, M. C. Wapler, U. Wallrabe, *Soft Matter* **2019**, *15*, 779.